Northumbria Research Link

Citation: Al-Nabulsi, Z., Mottram, J.T., Gillie, Martin, Kourra, N. and Williams, M.A. (2020) Mechanical and X ray computed tomography characterisation of a WAAM 3D printed steel plate for structural engineering applications. Construction and Building Materials. p. 121700. ISSN 0950-0618 (In Press)

Published by: Elsevier

URL: https://doi.org/10.1016/j.conbuildmat.2020.121700 <https://doi.org/10.1016/j.conbuildmat.2020.121700>

This version was downloaded from Northumbria Research Link: http://nrl.northumbria.ac.uk/id/eprint/44981/

Northumbria University has developed Northumbria Research Link (NRL) to enable users to access the University's research output. Copyright © and moral rights for items on NRL are retained by the individual author(s) and/or other copyright owners. Single copies of full items can be reproduced, displayed or performed, and given to third parties in any format or medium for personal research or study, educational, or not-for-profit purposes without prior permission or charge, provided the authors, title and full bibliographic details are given, as well as a hyperlink and/or URL to the original metadata page. The content must not be changed in any way. Full items must not be sold commercially in any format or medium without formal permission of the copyright holder. The full policy is available online: http://nrl.northumbria.ac.uk/policies.html

This document may differ from the final, published version of the research and has been made available online in accordance with publisher policies. To read and/or cite from the published version of the research, please visit the publisher's website (a subscription may be required.)

UniversityLibrary

Northumbria
University
NEWCASTLE

Construction and Building Materials xxx (xxxx) xxx

Contents lists available at ScienceDirect

Construction and Building Materials

journal homepage: www.elsevier.com/locate/conbuildmat

Mechanical and X ray computed tomography characterisation of a WAAM 3D printed steel plate for structural engineering applications

Z. Al-Nabulsi [a], J.T. Mottram [a,*], M. Gillie [b], N. Kourra [c], M.A. Williams [c]

[a] University of Warwick- School of Engineering, Coventry, United Kingdom
[b] Northumbria University, Newcastle upon Tyne, United Kingdom
[c] University of Warwick- Warwick Manufacturing Group, Coventry, United Kingdom

HIGHLIGHTS

- Construction industry can use WAAM 3D printed technology to optimise steel components.
- Mechanical properties are benchmarked against the material properties in Eurocode EN 1993–1-1.
- X-ray Computed Tomography is employed for quality insurance of the steel's integrity.
- Ductility of the WAAM steel limits this steel to static applications in building structures.

ARTICLE INFO

Article history:
Received 4 July 2020
Received in revised form 26 October 2020
Accepted 12 November 2020
Available online xxxx

Keywords:
Metal 3D printing
WAAM process
Mechanical properties
X-ray computed tomography
Tensile testing
Structural application

ABSTRACT

This paper reports an investigation to improve fundamental knowledge and understanding of 3D printing of steel in structural engineering. The process method examined is Wire and Arc Additive Manufacturing (WAAM) for the manufacturing of large-sized components. The mechanical properties of 3D printed Union K 40 - GMAW steel are determined and benchmarked against measured properties of EN 8 carbon medium steel. The results presented and discussed are from tensile coupon testing and X-ray Computed Tomography, with the latter inspecting an internal volume of the WAAM steel for: printing orientation; mapping porosity; interfacial variation between the printed layers. The key finding is that the mechanical properties of the WAAM steel satisfy the requirements for a structural steel grade for building structures as specified by Eurocode 3 (EN 1993–1-1).

© 2020 The Authors. Published by Elsevier Ltd. This is an open access article under the CC BY-NC-ND license (http://creativecommons.org/licenses/by-nc-nd/4.0/).

1. Introduction

Over the last three decades, the potential of 3D printing has evolved significantly, offering efficiencies and providing optimised structural solutions from the exploitation of this industrial revolution in manufacturing processing. Sakin and Kiroglu [1] observed in 2017 that 3D printing had become one of the fastest-growing technologies in manufacturing. Aerospace, oil and gas, marine and automobile applications were found by these authors to be attracting a lot of interest, because of flexibility and freedom in part design and enhanced product complexity for lightweight engineered solutions [2–4]. The next engineering sector to benefit from 3D printing is the construction industry [5]. Wu *et al.* [6] observed that 3D printing technologies can have significant benefits in reducing construction times; minimising costs for improved affordability; reducing waste; and increasing design flexibility.

There have been several 3D-printing projects that illustrate effective redesign as another benefit to the construction industry. For examples, for non-structural components previous projects include an 1.5 × 4 × 0.1 m aluminium window frame, with its steel/aluminium 0.25 × 0.3 × 0.01 m curtain wall bracket [7], and a 0.6 m wide and 0.8 m high nylon decorative joint to substitute an existing steel cladding connection [8]. To demonstrate the possibilities of Additive Manufacturing (AM) processing there are projects for scaled-down components, such as: 50 × 50 mm cross-section stainless steel sub-columns [9]; micro-lattice structures [10]; an optimised tensegrity node structure [11]; topology optimisation for stainless steel three-branch joints [12].

Using the capability of AM to print complex 3D shapes and its ability to print a component of more than one material enabled Izard et al. [13] to optimise a damper unit for civil engineering based on an optimised energy dissipation analytical model for

* Corresponding author.
E-mail address: Toby.Mottram@warwick.ac.uk (J.T. Mottram).

https://doi.org/10.1016/j.conbuildmat.2020.121700
0950-0618/© 2020 The Authors. Published by Elsevier Ltd.
This is an open access article under the CC BY-NC-ND license (http://creativecommons.org/licenses/by-nc-nd/4.0/).

Please cite this article as: Z. Al-Nabulsi, J.T. Mottram, M. Gillie et al., Mechanical and X ray computed tomography characterisation of a WAAM 3D printed steel plate for structural engineering applications, Construction and Building Materials, https://doi.org/10.1016/j.conbuildmat.2020.121700

achieving negative stiffness with significant energy dissipation. Another relevant enhancement is for the size of 3D printing components, with the 12 m span steel pedestrian bridge in the Netherlands [14] taking AM for construction to a new scale. To provide AM components for on-site construction applications, the company Autodesk has developed a mobile cabinet for Wire Arc Additive Manufacturing (WAAM) processing with steel welding materials [15].

Today, limitations that are potentially delaying routine field applications vary from the lack of technical information on the quality of the final 3D printed components to the detailed information for achieving the highest material quality from the printing processes themselves [16]. In addition, there is an absence for 3D printed steel components of standards (such as for the design of structures, see EN 1993–1-1:2005 [17]) and other guidance to benchmark/evaluate their structural performances as novel-shaped components over their intended design service lives.

The aim of this paper is to build confidence in WAAM produced 3D printed steel, which inherently uses a welded grade of steel, can create processing porosity, a rough surface and a non-homogeneous micro-structure. The new contribution will show that the welded steel possesses mechanical properties that can be in accordance with the material specifications found in Section 3 of the steel structural Eurocode BS EN 1991–1-1:2005 [17]. By demonstrating that WAAM steel does, indeed, possess materials properties that satisfy this Eurocode standard, it will be acceptable to employ, where appropriate to do so, the structural design procedures in the standard to design steel structures having WAAM components of relatively large sizes.

1.1. Printing metal and structural application

Fig. 1 shows the three stages of redesigning, enhancement, and construction to be employed for component optimisation when using 3D printing in civil engineering works. Often, the required components/structures for any construction project are known, and conventional manufacturing has, for many years provided cost-effective engineered solutions for construction with the materials of steel, concrete, timber, etc. With 3D printing the opportunity is present to redesign steel components and to offer the capability to manufacture steel components at sizes found in conventional steelwork structures. These major benefits are also enhanced by adding the potential advantages of: optimise structural shapes with complex geometries; printing-off bespoke and single components; employing automation; removing any requirement for highly skilled welders. To transfer all these AM advantages into structural engineering applications it is necessary to build confidence in AM technology, and to achieve this goal, research and development projects, like that reported in this paper, are on-going to fill-in known gaps to our current knowledge and understanding.

1.2. Wire Arc additive manufacturing (WAAM)

There are a variety of AM processes that the construction sector could apply during this early stage of application development [16]. AM methods for metal components can be split into the two technologies of either the Powder Bed Fusion (PBF) technology or the Directed Energy Deposition (DED) technology [18], being based on the source of energy and the input of raw construction materials as either metal powders (in PBF) or wires (in DED) [2,3].

To avoid having a lower limitation on maximum spatial dimensions, the DED process of WAAM is found to be more appropriate. Whereas, the component size manufactured by a PBF method is always limited by the process chamber size, the robotics arm (with six-axis motion) in the WAAM process can readily be programmed to 3D print complex and much larger components. Size is now simply limited by the size of the robot arm and/or the movement of the robot unit itself. Additionally, WAAM is not restricted to the limitations of an overhead gantry system mentioned in the literature [19,20], which involve issues for accessibility, especially on-site, and for transportation and installation on-site of the system. Other disadvantages of PBF 3D printing are that this AM method can require a sintering stage that is an extra processing/energy stage and its deposition rate of steel at 0.2 kg/hr is 45 times less than the 9 kg/hr achieved by DED processing [21].

The three photographs in Fig. 2 show the WAAM process equipment with Autodesk in the UK, where the heat source melts a steel wire being laid down by the robot. It is the combination of an electric arc and wire as feedstock which gives this DED process the name WAAM [22]. In the process the welding torch, seen in Fig. 2(a), dispenses the steel wire as molten metal at a specified rate, whilst moving in one direction (as shown by the yellow arrow) and builds-up a component's volume, first in the horizontal plane, and then in the vertical direction layer-by-layer. Although not relevant to the characterization work of the steel reported herein, it is important to understand that WAAM processing is well-suited for adding complex-shaped features into large components [2].

Taking a historical perspective on the development of iron-based materials, it is seen that cast iron [23] has similar physical feature to WAAM steels, such as: shrinkage, residual stresses, porosity, roughness of the surfaces and dimensional tolerances of final component (if no additional machining is employed). These similarities allow cast iron to be selected as a reference construction material because it has been successfully used in civil engineering structures.

The characterization work presented in this paper is used to investigate a WAAM produced steel by determining short-term mechanical tensile properties and obtaining the internal microstructure by using X-ray Computed Tomography (XCT) analysis. The non-destructive testing method provides a quality control characterization that can be used to establish a scientific association between the level of porosity and the steel's material properties, which are compared with those for steel grades scoped by the steel structural Eurocode BS EN 1993–1-1:2005 [17].

2. WAAM processing and steel sample

To 3D print the sheet of steel seen in Fig. 3, the processing parameters using the WAAM equipment, shown in Fig. 2, were guided by the manufacturer Autodesk. The wire of diameter

Fig. 1. Three steps in 3D printing toward optimised engineering solutions.

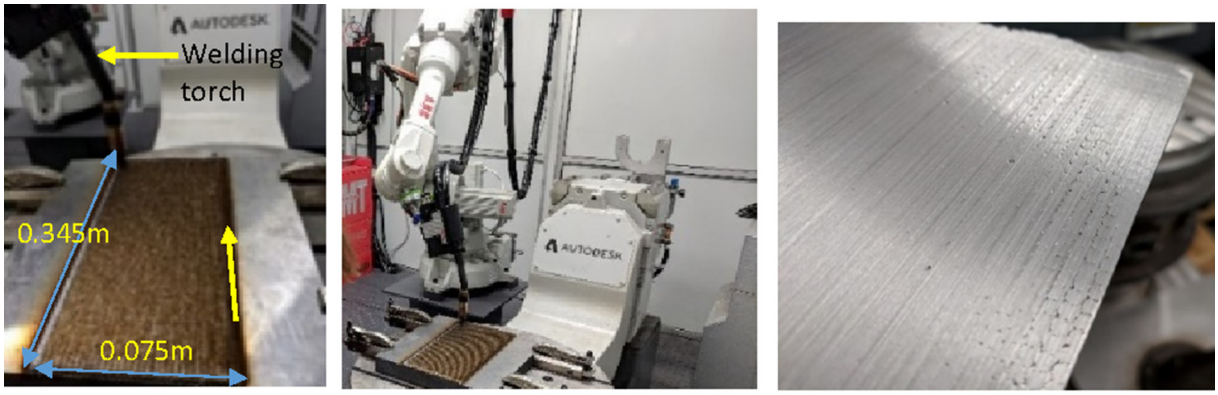

Fig. 2. (a) WAAM printing process; (b) WAAM Printer and robot arm; (c) WAAM flat sheet component.

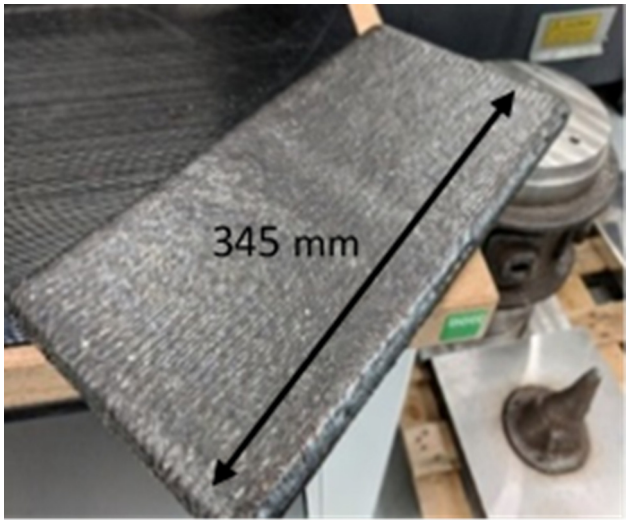

Fig. 3. WAAM 3D printed steel sheet of thickness 20.5 mm.

1.2 mm was type Union K 40. This is a Gas Metal Arc Welding (GMAW) solid steel wire, which according to the supplier has: a 25% strain at ultimate failure (ε_u); a yield strength (f_y) of 360 N/mm^2 at 0.2% proof strain (ε_y); an ultimate tensile strength (f_u) of 400 N/mm^2. GMAW solid wire electrode is often used for welding unalloyed and low alloy steels with shielding gas. This is because it is especially suited for electrolytically and hot dip galvanized thin sheets that are used primarily in vehicle and autobody fabrication.

For this research Autodesk printed a Union K 40 steel sheet component of dimensions 0.345 × 0.075 × 0.0205 m in approximately 10hrs of processing time. In the WAAM process the torch direction is always laid down parallel to the longer side length of the sheet (i.e. coinciding with the length 345 mm in Fig. 3), and this is the Longitudinal direction. There are five printed layers in building-up the plates' mean thickness to 20.5 mm. The word layer has the meaning that the volume of steel is continuous and homogeneous. At the interface between the five layers there is a change in the steel's composition and porosity is present (as identified by XCT imaging). Note that the thickness of the sheet is not constant with an overall surface roughness (which can be seen in Fig. 3), which is known to be dependent on the printing parameters, particularly the printing speed.

To evaluate the mechanical properties of the printed steel the authors decided to compare the measured properties against the equivalent material properties reported in Section 3 (Materials) in EN1993-1–1:2005 [17]. The reason for this is that if the 3D printed steel is shown to possess material properties that meet the specification of steel grades in Eurocode 3 so does the WAAM processed steel Union K 40. Note that Union K-140 is a welding steel and therefore does not necessarily have to possess the material properties to be a Eurocode 3 specified grade of steel. This paper reports on the test methods and test procedures to characterize the tensile properties and internal micro-structure using coupons cut from the sheet component shown in Fig. 3.

2.1. Machining and cutting for test sample geometries

Post-processing steps for the WAAM component could have varied between heat treatment, milling, grinding, machining, etc. One feature of WAAM printed components is that the outer surface is rough and for the Autodesk plate this roughness can be considered as the striation lines seen in Fig. 3. As seen in Fig. 4(a) a grinding wheel running at a fixed speed of 1650 rev/min was used to grind down the steel to a constant 17 mm thickness. The prepared plate has flat and polished surfaces, which are needed in tensile testing for gripping and to bond on post-yield rosette and axial strain gauges. Then, as seen in Fig. 4(b), three tensile dog-bone coupons were cut-out using an aqua jetting technique. Moreover, as identified by the blue ellipses in Fig. 4(c), four through-thickness rectangular coupons were cut-out-from the steel left in the sheet between the three tensile dog-bone coupons. This provided non-standard coupons to make a further examination of the steel having the interfacial regions from the 3D printing. Because the coupons did not receive a heat treatment process the material properties of the steel were determined including the WAAM processing residual stress distribution. It is worthy to note that post-processing heat treatments are expensive and time-consuming and for construction applications can be seen to be undesirable on cost grounds alone. Post 3D printing heat treatments might be necessary with AM components in other engineering sectors.

Figs. 5 and 6 show a dog-bone coupon based on standard BS EN 10002 [24], and a through-thickness (non-standard) rectangular coupon taken from the WAAM printed component. Table 1, with its accompanying Fig. 7, defines the dimensions for three different coupons. Column 1 is for coupon type and coupon labelling scheme, and columns 2 to 5 report in millimetres: thickness (a_o); width (b_o); gauge length (L_o), for part of coupon to measure the direct strain; parallel length (L_c), which for dog-bone coupons is larger than L_o; overall coupon length (L_t). First and second rows in Table 1 give the dimensions for both types of coupons of the WAAM steel. They have a size and geometry that was commensurate with the limited amount of available 3D printed steel (see

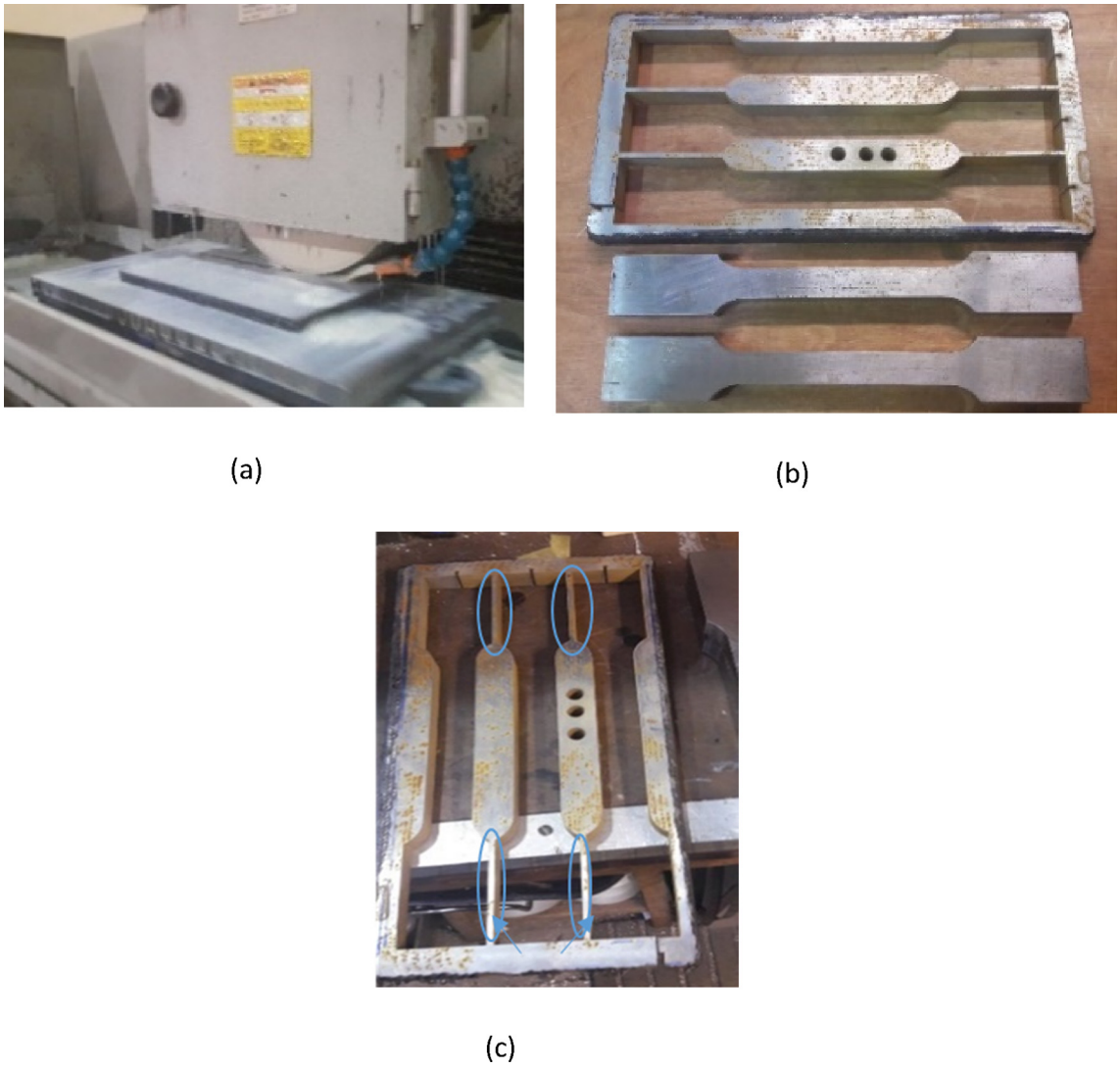

Fig. 4. Coupon preparation: (a) grinding processing of sheet in Fig. 3; (b) tensile dog-bone coupons and remaining part of sheet; (c) locations for extracting the through-thickness coupons.

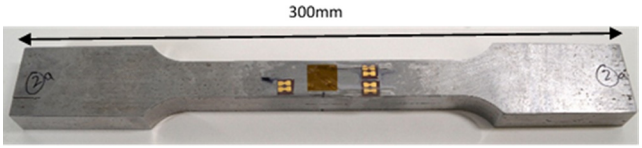

Fig. 5. tensile coupon specimen WAAM_L_T_2 with strain gauging.

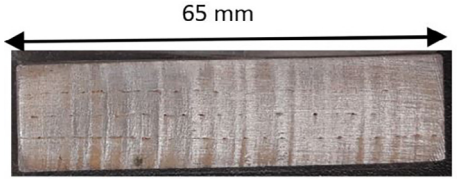

Fig. 6. Through-thickness coupon.

sheet in Fig. 3). The dog-bone coupons (see Fig. 7) were sized following the proportional test method where the gauge length (L_o) is related to the original cross-section area (A_o), by the formula $L_o = 5.65\sqrt{A_o}$. [24]. The overall length of the specimen was limited to the printed thickness, after grinding, which is 17 mm, and to the chosen coupon width for the rosette strain gauging. Accordingly, for WAAM_L_T coupons the minimum L_o for the 20 × 17 cross-section is 104 mm, and for the maximum coupon length of 300 mm the parallel length (L_c) is 132 mm.

The labelling of the dog-bone coupons is WAAM_L_T_1, where 'L' is for Longitudinal (wire laying down) direction. 'T' for Tensile testing and '1′ is for coupon number 1. The only change with the non-standard coupons is that 'L' is replaced with 'TT' for the Through-Thickness direction, which is for when the axial strain gauging is positioned on the 'thickness' surfaces, noting that the direction of tensile load is still in the Longitudinal direction.

To provide a benchmark material a single tensile dog-bone coupon was prepared of EN 8, a medium carbon steel, also having dimensions in accordance with the proportional test approach in BS EN 10002 [24]. The third row in Table 1 shows that for the EN_8 coupon the mean cross section was 10 × 20 mm.

3. Test set-up and test procedure

Tensile testing was performed to determine the direct stress-direct strain relationship of the steels to ultimate failure. As

Table 1
Dimensions for the coupons with reference to geometrical variables defined in Fig. 7.

Coupon type and labelling scheme	Thickness and width ($a_o \times b_o$) mm	Gauge length (L_o) mm	Parallel length (L_c) mm	Length (L_t) mm
1	2	3	4	5
WAAM_L_T_1 to 3 (dog-bone)	17 × 20	$5.65\sqrt{340}$ = 104	104.2 + $1.5\sqrt{340}$ = 132	300
WAAM_TT_T_1 to 4 (straight sided)	3.8 × 17	$5.65\sqrt{64.6}$ = 45	65	65
EN_8 (dog-bone)	10 × 20	$5.65\sqrt{200}$ = 80	80 + $1.5\sqrt{200}$ = 101.5	300

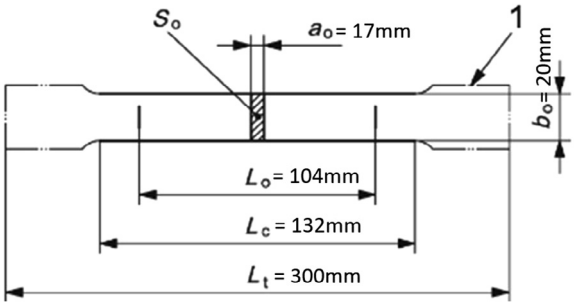

Fig. 7. Standard tensile coupon geometry [24].

Fig. 8(a) shows testing consisted of a WAAM_L_T coupon with longitudinal and biaxial YEFRA-5 post yield strain gauges, having a strain limited of 10 to 15% (see Fig. 5) and bonded using a compatible CN-Y cyanoacrylate adhesive, external extensometers and a 250kN Instron universal testing machine. Test results were recorded in real time using a Model 800–8-SM data acquisition system that filtered and record strains synchronised with the tensile load impulses from the Instron. Readings from a 2630–118-105 longitudinal extensometer having gauge length of 80 mm and an I3575-250 M transverse extensometer having gauge length of 20 mm were recorded in real time using BlueHill software (V 3.76.4926 (kN)) for the WAAM_L_T_1 to 3 and EN_8 coupons.

In the case of testing the non-standard rectangular coupons of WAAM_TT_T_1 to 4 elongation for direct strain was measured by a 2620–602-200700 axial dynamic extensometer having a 12.5 mm gauge length, with a travel of ±5mm giving ±40% strain (see Fig. 8(b)). Load was now applied using a 100 kN Instron universal testing machine.

For the maximum coupon cross-section size of 20 × 17 mm (see Table 1) and an ultimate tensile strength of 440 N/mm^2 (Union K 40 steel) the expected ultimate tensile load is 150 kN.

To validate the test set-up and procedure before proceeding to characterise the WAAM steel a benchmark test was performed using the same test procedure with the coupons of EN 8 steel.

The test procedure for the strength testing was in accordance with BS EN 10002 [24]. The constant stroke rate was 2 mm/min for the recommended 0.00025s^{-1} strain rate over the elastic stage for determination of both the upper yield strength (R_{eH}) and the tensile strength (R_m), which are for strengths f_y and f_u, respectively in EN1993-1–1:2005 [17]. Testing was performed at 23.5 °C and 34% humidity and the test duration was 17 min.

To inspect the WAAM steel's integrity and identify internal micro-structural changes the non-destructive, non-contact examination employed was X-ray Computed Tomography (XCT). Other techniques have been used in the past for the examination of AM components, one being radiography and liquid penetrate inspection [25]. XCT was chosen in this study because it has the main advantage of establishing the volumetric identification of differences in steel materials.

The test procedure utilises a series of digital radiographs from a full rotation of the examined sample that are reconstructed to create a 3D computational volume of internal and external geometries based on the attained grey values. XCT is uniquely able to segment the different internal regions according to achieved attenuation and provide volumetric analysis. As shown in Fig. 9 for the WAAM steel (after the sheet was grinded) the grey values variations presents regions of different steel composition with a higher atomic number with brighter grey values and regions of material with a lower atomic number with darker grey values. In the figure, the black regions are identified as internal voids where, at the

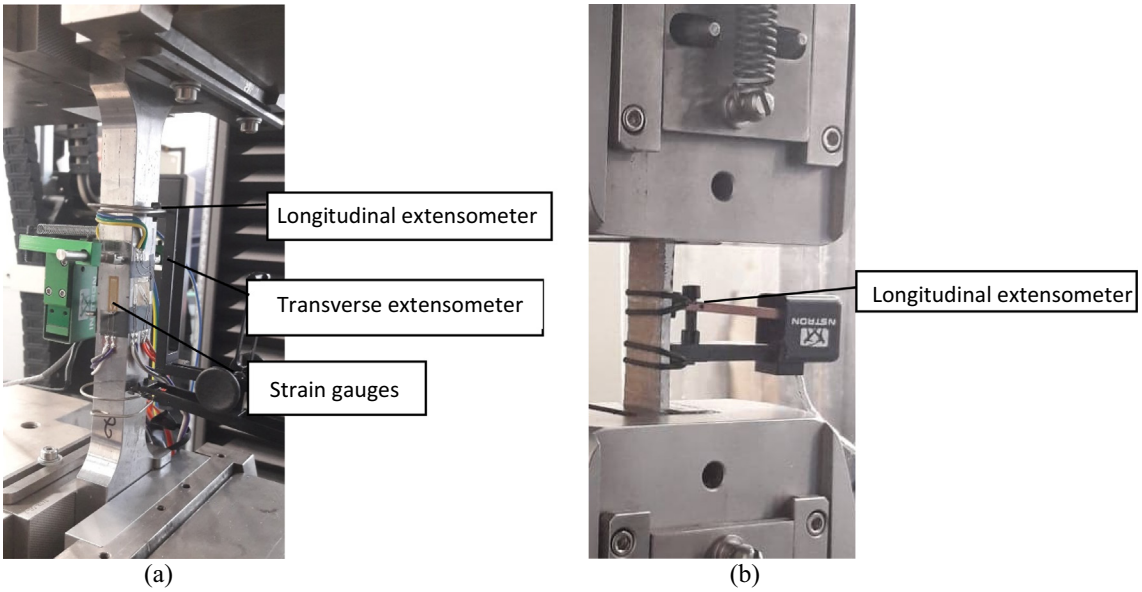

Fig. 8. Instrumented coupon in grips of an Instron testing machine: (a) dog-bone coupon; (b) rectangular coupon.

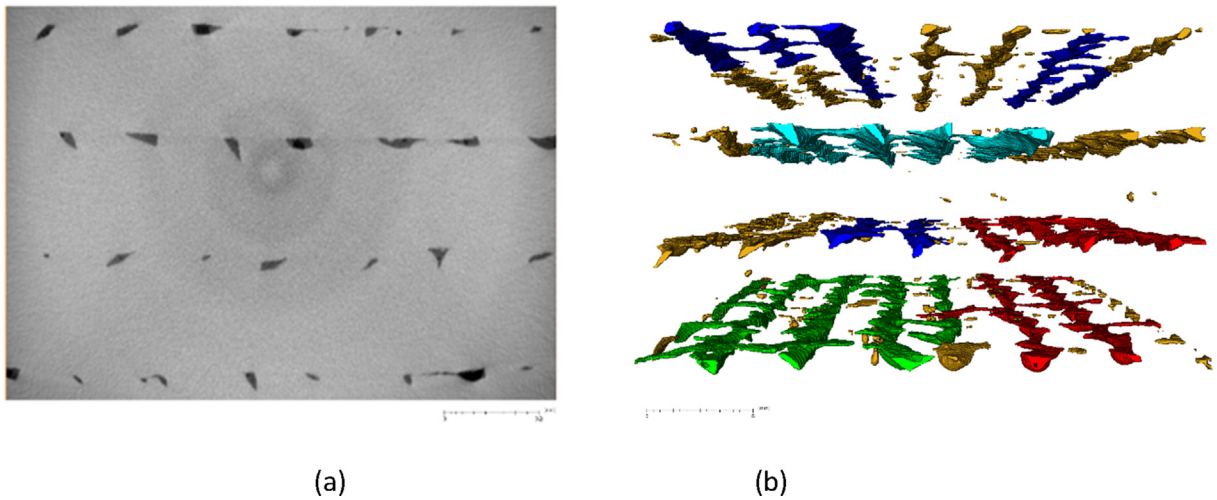

Fig. 9. XCT images of unstressed WAAM steel (there is approximately 3.8 mm of thickness between the layer interfaces). (a) grey-image through thickness; (b) coloured-image show porosity distribution at interfacial layers and in the Longitudinal direction.

interfaces of the five layers, the molten steel has not fully coalesced during the WAAM welding process. The grey-image in Fig. 9 is affected by common ring artefacts that do not limit the segmentation of the different regions. The coloured image on the right-side highlight the concentration of porosity in layers that exists at the interfaces separated by 3.8 mm in the thickness direction.

The XCT scanning of the coupons before and after tensile testing can expose any changes in the internal micro-structure owing to failure deformations; especially, at the interfaces where the porosity exists (see Fig. 9(b)). This highlights the link of how the WAAM steel responses to tension and the material's short-term material properties. To provide a benchmark on the quality of XCT scanning, a sample of EN-8 steel was used to establish a reliable contrast [26]. The calibrated procedure presented in [27] and [28] was used to minimise, if not eliminate the uncertainty regarding the known XCT limitations, such as signal noise.

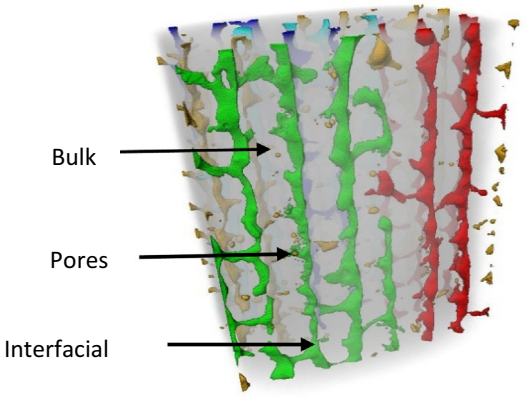

Fig. 10. Internal composition of WAAM steel plate by XCT.

4. Results and discussion

4.1. X-ray Computed Tomography (XCT)

XCT scanning provided valuable information in order to understand the internal micro-structure of the WAAM steel. Three types of samples were involved in this non-destructive evaluation, namely the dog-bone coupons before and after tensile testing (Section 4.2), and the through-thickness coupons, but only after testing.

As Fig. 10 shows the layered structure of the WAAM steel comprises of three constituents at different volume regions. The grey coloured region demonstrates the bulk homogeneous Union-40 K steel, which is the principal constituent. The green, red and blue coloured volumes in the figure are for interfacial regions between the five layers for the specific WAAM welding process. The final constituent is the voids (porosity) at the interfaces and is imaged by the beige coloured discontinuous volumes in Fig. 10. The porosity constituent has the lowest volume fraction of the three.

Figs. 11 and 12 show the 3D volume of WAAM steel before tensile testing that were used to calculate the volume fraction of porosity. For the interfacial regions seen in Fig. 11 the 3D printing parameters used by Autodesk does not allow the molten steel to fully coalesce, and this processing weakness can be due to the inter-passing distance parameter of the weld torch (see Fig. 2(a)). The XCT scanning highlights that steel in the interfacial region can have a slightly lower density than that of the bulk of the steel. Fig. 12 shows further that along these interfacial regions there are pockets of porosity where there is no steel present.

A volumetric analysis of the WAAM steel before tensile testing finds that the mean volume fraction of porosity is 0.1%, while the volume fraction of the regions of steel having the lower density is 1.68%. Archimedes principle can be applied to determine average steel density. A precision electronic balance was used with a built-in hook from which the WAAM_L_T_1-3 coupons were individually hung to measure, in air, their weight to 0.01 g. Next, the balance was zeroed before lowering the coupon to be submerged underwater. A minus weight reading was now recorded to give the coupon's volume. Taking into consideration any change in temperature [29], the average calculated density from three coupons is 7.77 g/cm^3. This gives a 0.7% difference to the recognised density of medium carbon steel (EN-8) for the benchmark steel material.

Archimedes principle was further employed to establish the porosity volume fraction. Researchers [26] highlighted its potential to capture a reliable measure of porosity, in addition to its capacity for determining material density. Spierings *et al.* [30] mention that the method has a limitation because it produces a higher value than the actual level of porosity. The presence of this limitation could be justified owing to low resolution in capturing the porosity and noting the presence of denser regions of steel away from the interfacial regions.

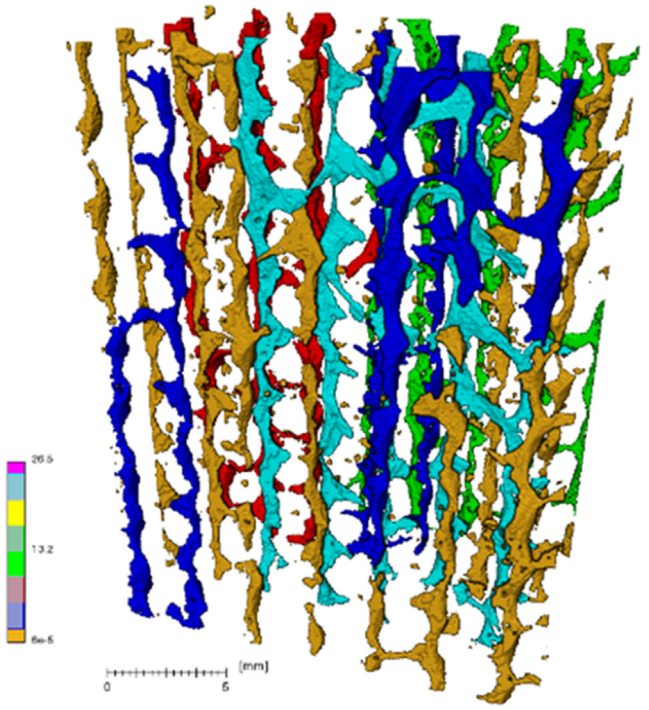

Fig. 11. Volumes at the interfacial regions having lower steel density (colours according to volume sizes).

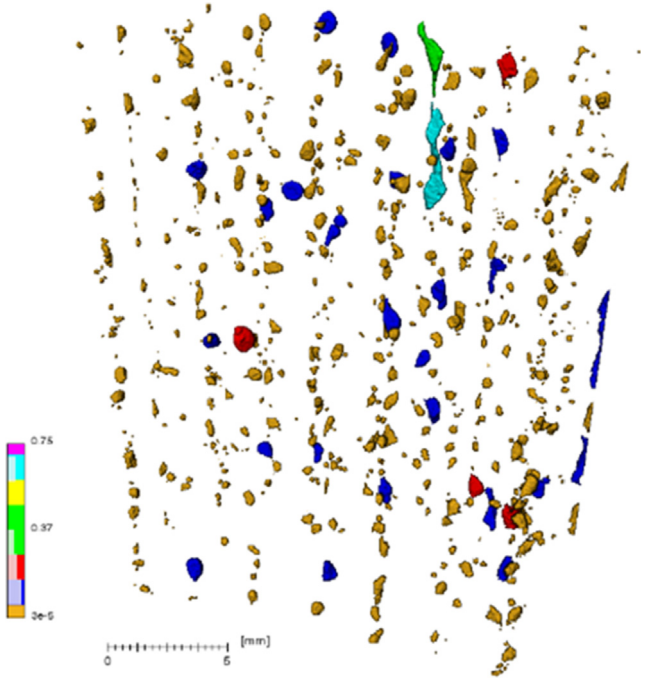

Fig. 12. Pores distribution in the WAAM steel (colours according to their volume size).

Reported in Table 2 are the volume fraction of the three constituents in the WAAM steel, determined after tensile testing. Column 1 defines the three constituents (see Fig. 10), with (A) for bulk steel, (B) for interfacial regions, and (C) for porosity. Columns (2) to (4) lists the volume fractions as percentages for the three constituents. It is observed that the percentage of interfacial regions is from 0.38 to 0.64%, with a mean of 0.48%. Furthermore, the analysis finds that the porosity ranges from 0.05 to 0.21%, and because the through-thickness coupons are relatively small (refer to Table 1), their higher porosity indicates that there can be localised differences in the amount of porosity. This preliminary finding might be reflected in localised differences in material properties observed in the tensile test results presented in Section 4.2.

Table 2
Volume fractions of the three media in WAAM steel after tensile testing.

	Volume fraction (%)		
Medium	WAAM_L_T_1	WAAM_L_TT_1	WAAM_L_TT_2
1	2	3	4
Bulk steel (A)*	99.52	99.42	99.24
Interfacial regions (B)	0.43	0.38	0.64
Porosity (C)	0.05	0.21	0.12

Figs. 13 and 14 show the XCT volumes of WAAM_L_TT_1 and WAAM_L_TT_2 after fracture. The interfacial regions are exposed in Figs. 13(a) and 14(a), giving evidence for a homogenous deformation throughout the coupon cross-section. Note that the fracture occurs at the top of the volume where there is the cup and cone fracture zone. In Figs. 13(b) and 14(b) the interfacial regions are shown to have the lower density steel combined with the porosity. The porosity alone is shown in Figs. 13(c) and 14(c). Coupon photographs in Figs. 13(d) and 14(d) show the regions covered by the XCT scanning. From the images in Figs. 13(c) and 14(c), it can be observed that the fracture deformation occurred close to the top where the prominent voids are elongated. It can be speculated that the stress concentrations at one or more voids might have led to premature fracture in the steel with a lower fracture strain (ε_u) than its value would have been had there been no porosity. The level of importance of the XCT scanning test results is discussed after the tensile coupon test results are reported and discussed in Section 4.2.

An important lesson to be learnt from the XCT characterization work is that by using the WAAM processing parameters in this study there are voids (to volume fractions of 0.2%) within the interfacial region. Because porosity lowers mechanical properties, particularly under fatigue loading, we want to eliminate it, if practical to do so, by establishing the optimum processing parameters. Further work is therefore necessary with the WAAM processing parameters to find out what is the minimum possible percentage of porosity.

4.2. Tensile tests

Prior to presenting and discussing the WAAM steel tensile test results, it is relevant to present the material properties of structural steel for the design of steel structures informed by the code of practice, known as Eurocode 3, BS EN1993-1–1:2005 [17]. Specific steel grades are listed that satisfy parts of the standard BS EN 10025 for hot rolled products of structural steels [31]. Note that the tensile properties of these steel grades are to be determined in accordance with BS EN 10002 [24]. These steels are for a thickness $\leq$ 40 mm and for various section shapes. The range of characteristic yield strengths (f_y) is from 235 to 460 N/mm^2 and characteristic ultimate tensile strengths (f_u) is from 360 to 570 N/mm^2; the higher the yield value the higher is the ultimate value. Section 3 then provides in paragraph 3.2.2(1) the ductility requirements. These requirements are expressed as follows.

For steels a minimum ductility is required that should be expressed in terms of limits for:

– the ratio f_u / f_y of the specified minimum ultimate tensile strength fu to the specified minimum yield strength f_y;

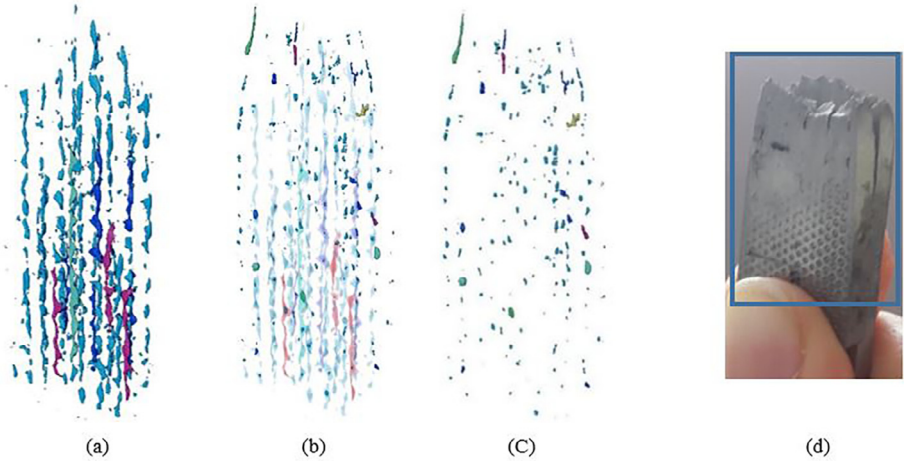

Fig. 13. Internal structure of fractured coupon WAAM_L_TT_1: (a) interfacial regions; (b) interfacial regions and porosity; (c) porosity distribution. (d) blue box is for region of coupon with XCT imagining. (For interpretation of the references to colour in this figure legend, the reader is referred to the web version of this article.)

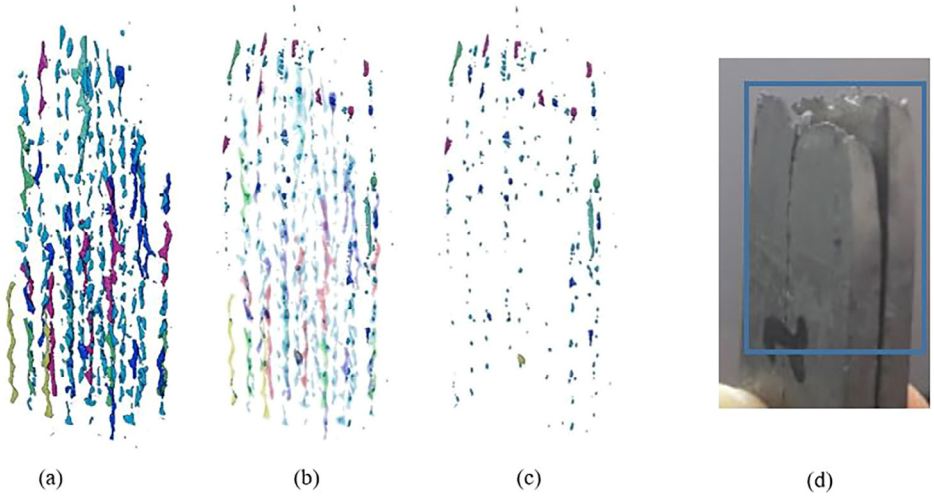

Fig. 14. Internal structure of fractured coupon WAAM_L_TT_2: (a) interfacial regions; (b) interfacial regions and porosity; (c) porosity distribution, (d) blue box is for region of coupon with XCT imagining. (For interpretation of the references to colour in this figure legend, the reader is referred to the web version of this article.)

- the elongation at failure on a gauge length of $5.65A_o$ (where A_0 is the original cross-sectional area);
- the ultimate strain ε_u, where ε_u corresponds to the ultimate strength f_u.

Beneath the paragraph is the note to state that for the limiting values of the ratio f_u/f_y, the elongation at failure and the ultimate strain ε_u may be defined in the National Annex. In the British Standard (BS) Annex [32] the following is recommended:

For buildings the limiting values for the ratio f_u/f_y the elongation at failure and the ultimate strain ε_u are given below.

- Elastic global analysis: $f_u/f_y \geq 1.10$; Elongation at failure not less than 15%; $\varepsilon_u \geq 15\varepsilon_y$.
- Plastic global analysis: $f_u/f_y \geq 1.15$; Elongation at failure not less than 15%; $\varepsilon_u \geq 20\varepsilon_y$.

For bridges plastic global analysis should not be used and the limiting values for the ratio f_u/f_y, the elongation at failure and the ultimate strain ε_u for elastic global analysis are given as: $f_u/f_y \geq 1.20$; elongation at failure not less than 15%; $\varepsilon_u \geq 15\varepsilon_y$.

For the purpose of carrying out design calculations paragraph 3.2.6 recommends that the elastic constants are 210000 N/m^2 for the (mean) modulus of elasticity and 0.3 for Poisson's ratio.

In BS EN 1993–1-1 Section 3 [17] there are material property requirements for fracture toughness, through-thickness properties that are not considered in this study.

Plotted in Fig. 15 are tensile direct stress-direct strain curves to ultimate failure, coloured blue, red and black, for the test results from coupons WAAM_L_T_1 to WAAM_L_T_3. Also plotted in the figure is a purple coloured curve for the benchmarking characteristics from testing coupon EN_8 (see Table 1). Inspection of the test results show that the WAAM steel curves have similar ductile-steel characteristics as the benchmark medium carbon grade steel.

Reported in Table 3 are the individual test results for coupons WAAM_L_T_1 to 3. In this table, column 1 is for the coupon labels and names of statistical properties. The modulus of elasticity, E, is given in column 2 and this property was calculated from the slope to 65% of the linear (elastic) part of the direct stress-direct strain curves plotted in Fig. 15, using the least squares fit method. Columns 3 and 4 are for values of yield strengths. Column 3 is for the Eurocode f_y value that is equal to the upper yield strength

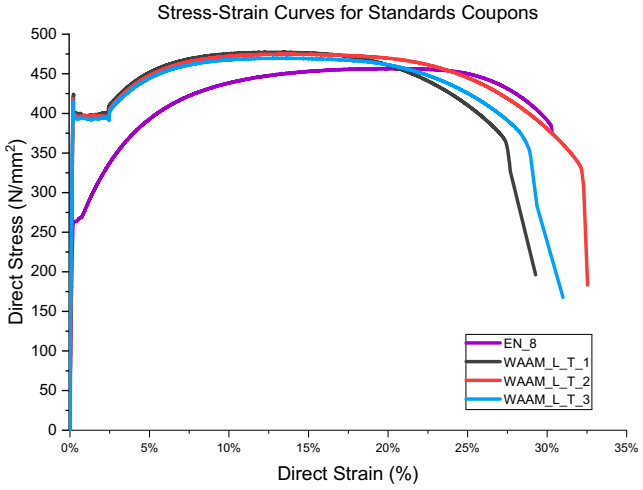

Fig. 15. Plots of direct stress against direct strain for dog-bone coupons WAAM_L_T_1 to 3 and EN8_1.

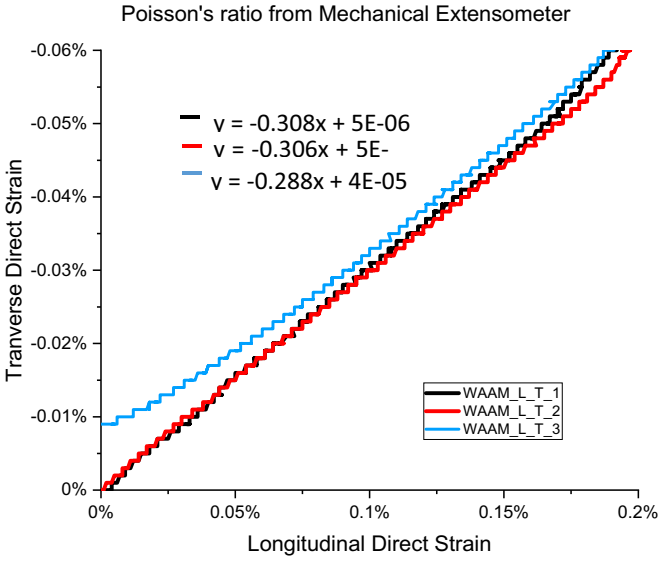

Fig. 16. Plots of transverse against longitudinal direct strains for the determination of Poisson's ratio for WAAM steel.

(or R_{eH} in EN 10002 for the first peak in the elastic zone before a decrease in stress). Columns 4 and 5 lists ultimate values for strength and strain. The Eurocode f_u value in column 4 is also R_m in EN 10002, and is the stress corresponding to the maximum tensile force recorded. In column 5 there is the corresponding direct ultimate strain ε_u.

Below the three rows in Table 3 with listings of the coupon's individual test results are four rows for the batch results of: mean; standard deviation for a normal (Gaussian) distribution (SD); Coefficient of Variation (CoV); characteristic value. Note that the mean value of the modulus of elasticity is also its characteristic value. For strength and strain properties, the characteristic values are obtained in accordance with paragraphs in Annex D of EN 1990 [33], by using characteristic value equal to mean minus n times SD, where SD is the standard deviation. For three coupons in the batch n is equal to 1.89. Because the CoV is always <10% for properties reported in columns 3 to 6 there is justification to calculate the characteristic value with the assumption that the coefficient of variation is known a priori [33]. If a coefficient of variation had been >10% then n could be taken as 3.37 and the calculation of characteristic values will be lower.

From the tensile test results, the mean yield strength (f_y) is 419 N/mm^2 (CoV of 1.1%) at a mean yield strain (ε_y) of 0.21% (not reported in Table 3 because it is a constant). The mean ultimate strength (f_u) is 474 N/mm^2 (CoV of 0.8%) at a mean ultimate strain (ε_u) of 13.3% (CoV of 2.8%), with the strain at fracture (ε_f) higher than 26% (CoV of 6.8%). These values are higher than reported in Section 2 from the supplier for the Union K 90 wire used to 3D print the steel sheet seen in Fig. 3. The mean modulus of elasticity is 20800 N/mm^2 (CoV of 8.0%), which is 1.4% lower than its specified mean value in Eurocode 3 [17]. The reason for this is the relatively low E of 189000 N/mm^2 measured from coupon WAAM_L_T_3; 216000 N/mm^2 is the mean taking results from the other two dog-bone coupons.

From Table 3 it is seen that the characteristic strengths f_y = 411 N/mm^2 and f_u = 467 N/mm^2 of the WAAM steel fall within their, respective, Eurocode 3 [17] ranges from (f_y) 235 to 460 N/mm^2 and (f_u) 360 to 570 N/mm^2. Note that the CoV is close to 1%, showing that for a coupon having cross-section size 20x17mm there is low variation in strengths. Because the ratio f_u/f_y = 1.14 the WAAM steel can be deemed acceptable as a steel grade in accordance with the ductility requirements of f_u/f_y = 1.15 in BS EN 1993–1-1 [17] for plastic global analysis for design of buildings or bridges. Elastic global analysis is verified only for buildings because elongation at failure, ε_f = 26% is greater than 15%. Also, the remaining ductility requirement ε_u = 12.7% $\geq$ 15 $\times$ ε_y = 3.15% is satisfied. It is noted that for the measurement of strain by an extensometer, the gauge length with WAAM_L_T coupons is 80 mm. This length should have been 104 mm (Table 2) so that the elongation at failure is measured over a desired gauge length equal to 5.65A_o. It is believed that this transgression from the requirements of Section 3 in BS 1993–1-1, because of the limited size of the WAAM sheet at 0.345 $\times$ 0.075 m, did not affect the findings described herein because the tensile strain values are much higher than their minimum requirements.

Combining readings from the axial and transverse extensometers and the bi-axial strain rosettes, Poisson's ratio was determined and is presented in Fig. 16 as the gradient to the transverse strain

Table 3
Material properties for WAAM steel determined using proportional dog-bone coupons and test method BE EN 10002 [24]

	Material property				
	E (N/mm^2)	f_y (N/mm^2)	f_u (N/mm^2)	ε_u (%)	ε_f (%)
1	2	3	4	5	6
WAAM_L_T_1	219,000	424	477	13.0	27.5
WAAM_L_T_2	216,000	419	475	13.7	30.9
WAAM_L_T_3	189,000	415	470	13.5	28.7
Mean	208,000	419	473	13.4	29.0
Standard deviation	16,500	4.51	3.61	0.36	1.72
Coefficient of Variation (CoV)	8.0	1.1	0.8	2.8	6.7
Characteristic value	177,000	411	467	12.7	25.8

against longitudinal strain. Coupons WAAM_T_L_1 to 3 gave a constant Poisson's ratio of mean 0.30; this is same value as from paragraph 3.2.6 for design values of material coefficients in Eurocode 3 [17].

Four further tensile stress–strain curves are reported in Fig. 17 from testing with the non-standard rectangular coupons WAAM_L_TT_1 to 4. Note that compared to the WAAM dog-bone coupons of cross-section 17 × 20 mm (Table 1) these coupons had a cross-section size of 3.8 × 17 mm, and thereby a thickness 4.47 time greater than width and a cross-sectional area five time lower. Plotted in the figure are four curves, coloured yellow, green, blue and mauve, and for comparison the single purple coloured tensile characteristics from coupon EN_8. From the four rectangular WAAM coupons the mean yield strength is 375 MPa at mean strain of 0.2% and the mean ultimate strength is 454 N/mm^2 at a mean ultimate strain of 12.7%. Although the mean strain at yielding is the same, the yield strength is 44 N/mm^2 lower than determined using the WAAM_L_T_1 to 3 dog-bone coupons. It is also seen that the mean ultimate strength is 20 N/mm^2 lower. Because these coupons are straight-sided and non-standard their test results are not used to determine characteristic values for a comparison with material properties in Eurocode 3.

It is seen from the four plots in Fig. 17 that there is consistency in the steel's response for coupons WAAM_L_TT 1 to 4 to a strain of about 14.6%. Plastic deformation with ductile fracture is the same failure mode as the tension stress goes beyond the elastic limit. Fig. 18(a) to (c) shows that fracturing in both dog-bone and non-standard coupons is by the well-known cup and cone failure mechanism of a ductile steel. It is found that the mean reduction in cross-section area is 53% for WAAM_L_T1 to 3, 40% for WAAM_L_TT_1 and 2 and 30% for WAAM_L_TT_3 and 4. The lower is the reduction in area the lower is the ultimate strain at fracture as seen from the results in Figs. 15 and 17. The practical reason why the fracture strain recorded with coupons WAAM_L_TT_3 and 4 does not exceed 15% is that the cup and cone failure did not occur in the 12.5 mm length of the extensometer. In other words, ε_f was not measured by the extensometer, only tensile deformations to a plastic strain of about 12%, prior to the localized cup and cone failure elsewhere. Fig. 17 shows the falling branch for these two coupons (blue and brown coloured curves). By connecting together the two fractured part ε_f was measured for WAAM_L_TT_3 and 4 to be 18% and 21%, respectively.

Plotted in Fig. 19 are the seven WAAM steel coupon test results (without fracture strains for WAAM_L_TT_3 and 4) to highlight differences in ε_f, the strain at fracture. Stress–strain curves can be divided into having the following three main stages of: linear elastic: strain hardening: steel fracture. Coloured curves black, red and blue are for coupons WAAM_L_T_1 to 3 and show similarities in the first two stages, while a divergence starts with the onset of the falling branch and recorded ε_f.

It is known [34] that internal molecular equilibriums are associated with the plastic flow balance between the stages of the tensile stress–strain relationship under uniaxial load. Eudier [35] has found that the existence of porosity has great effect on reducing the fracture strain and for decreasing the yield strength. Additional evidence for how porosity affects steel material properties is given in the literature for cast steel. Hardin and Beckermann [36] showed that stiffness depends on the size and distribution of voids, and in [37] that porosity also has an impact on the fracture mechanism during the ductile fracture stage.

Now inspecting the WAAM_L_TT_1 to 4 results in Fig. 19, given by the green, purple, yellow and blue curves, a greater variation can be observed in all three stages aside from the elastic slope (for the modulus of elasticity). The new insight gained from this characterization work raises the question whether the material properties of f_y , ε_y, f_u and ε_u are affected by the presence and distribution of voids, and a possible greater localised non-homogeneity in the through-thickness coupons? Figs. 13 and 14 demonstrate the internal structure of coupons WAAM_L_TT_1 (having 0.21% of porosity) and 2 (having 0.12% of porosity) by XCT scanning, showing that local to the section of the coupon with the cup and cone fracture the voids are elongated. Now from an inspection of the falling branches in Fig. 19, leading to ε_f, there is evidence to suggest that this material property might be dependent on the size and the distribution of porosity, and that because the curves from coupons WAAM_L_T_1 to 3 are similar there can

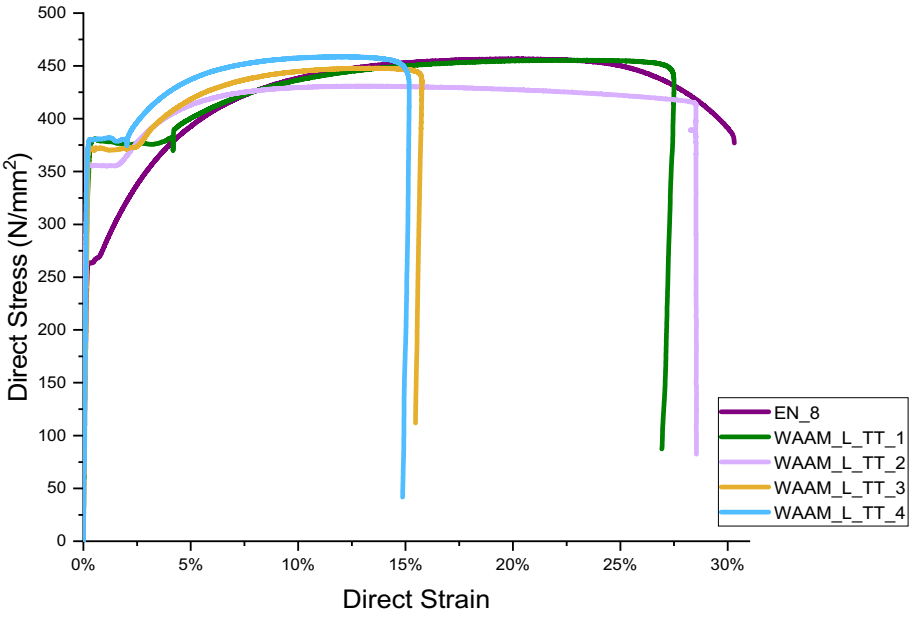

Fig. 17. Plots of direct stress against direct strain for non-standard straight-sided coupons WAAM_L_TT_1 to 4.

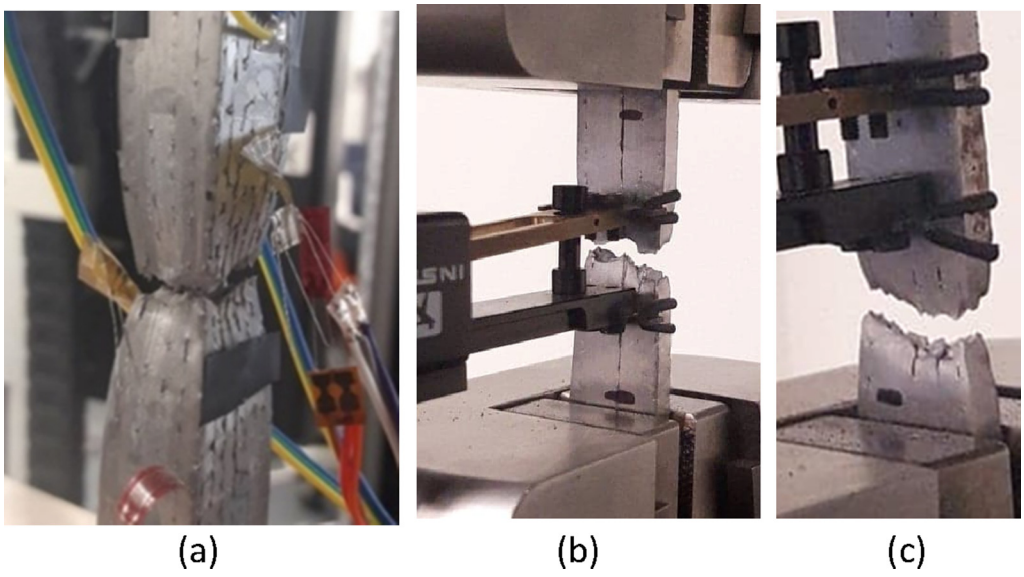

Fig. 18. Ductile cup-and-cone failure with coupons: (a) WAAM_L_T_3; (b) WAAM_L_TT_1; (c) WAAM_L_TT_3.

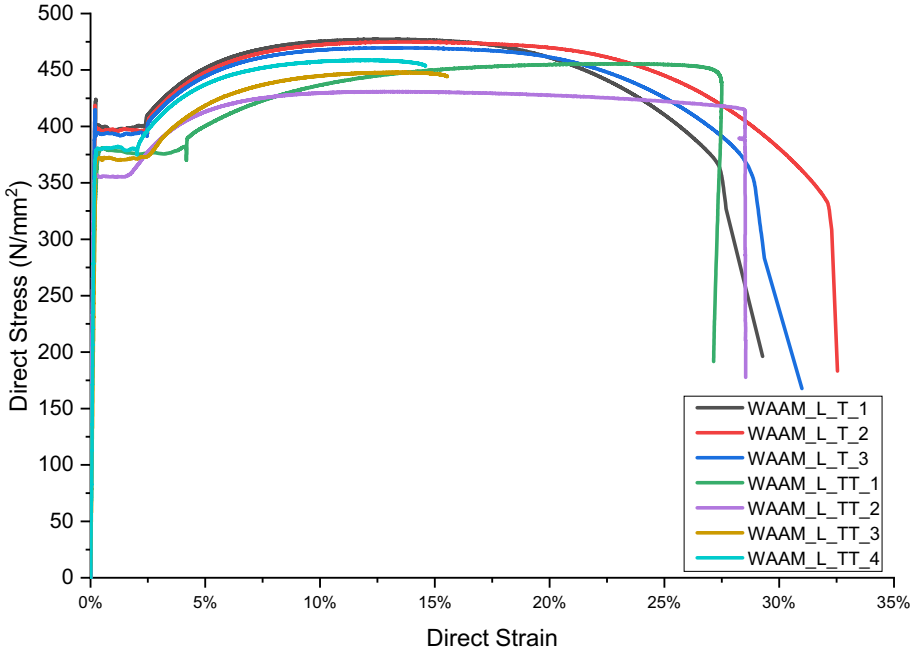

Fig. 19. Tensile test results combining the two batch test results in Figs. 15 and 17.

be a coupon size effect. It is possible from the results of this preliminary investigation to say that either an individual void or group of voids close together might have altered the flow distribution during plastic deformation causing fracture to occur in the WAAM_L_TT coupons. Hardin and Beckermann [37] suggest that when porosity is less than a few percent there is no measurable loss of stiffness, or large stress concentrations, or stress redistribution, but it will significantly reduce the fatigue strength. To verify the findings for steels made by WAAM additive manufacturing, a tensile testing programme is required to consider WAAM processing variables, and which satisfies standard BS EN 10002, including having a minimum dog-bone coupon batch size of five.

5. Concluding remarks

From the armoury of 3D printing technologies for additive manufacturing, the directed energy deposition process of Wire Arc Additive Manufacturing (WAAM) is employed to print a 20.5 mm thick sheet of Union K 40 - GMAW steel. After grinding-off the inherent surface waviness, several coupon specimens of 17 mm thickness were prepared to characterise the short-term tensile material properties of the WAAM steel. To examine the internal micro-structure formed during the welding process the non-destructive test method of X-ray Computed Tomography (XCT) was used with coupons prior to and after tensile testing.

Observations drawn from evaluating the new test results have started to fill-in known gaps in knowledge and understanding that are needed to prepare guidelines to design and execute optimum 3D steel printed components for building structures.

The main findings from the characterisation work are that:

- a steel sheet of 20 mm thickness can be 3D printed using the Autodesk equipment for the WAAM processing method.
- the material test results provide information for: the constitutive tensile stress–strain relationship; Poisson's ratio; the cup-and cone failure mechanism. All results are for a similar steel to the ductile characteristics of steel grades that satisfy the design requirements in the British version of the steel structural Eurocode, which is BS EN1993-1–1.
- the Union K 40 - GMAW steel in the 3D Printed sheet has an overall elongation that satisfies the requirement in BS EN 1993–1-1:2005.
- from mean properties the ratio of ultimate tensile strength to yield tensile strength at 1.14 is nearly in accordance with the minimum limit of 1.15 specified in the National Annex to BS EN 1993-1–1:2005:2008, which means the WAAM steel in this test is only valid for building structures designed by structural global analysis in the elastic range.
- XCT scans provide a quality control characterization of the 3D printed steel and information from the images may be used to develop a scientific association between the level of porosity and the steel's tensile properties.
- an important lesson to be learnt from results of XCT scanning is that by using the study's WAAM processing parameters there are, within the interfacial regions, pores have volume fractions of 0.2%.
- because the highest quality of WAAM steel will possess no porosity further work is necessary with variants to the WAAM processing parameters to find out if 0.2% is the minimum practical volume fraction of porosity.

It is the authors' expectation that the results from this research should be a step forward toward assist progress in applying WAAM processing of steel to manufacture building components that improve aesthetics and structural optimisation. This aim can, potentially, be achieved by applying additive manufacturing to redesign, enhance and construct new engineered solutions in order to use less steel and minimise embodied energy.

CRediT authorship contribution statement

Z. Al-Nabulsi: Conceptualization, Methodology, Formal analysis, Visualization. **J.T. Mottram:** Supervision, Conceptualization, Visualization. **M. Gillie:** Supervision. **N. Kourra:** Scanning Method, Formal analysis, Conceptualization. **M.A. Williams:** Supervision.

Declaration of Competing Interest

The authors declare that they have no known competing financial interests or personal relationships that could have appeared to influence the work reported in this paper.

Acknowledgements

The first author thanks both The School of Engineering (SoE) and The University of Warwick for financially supporting her PhD studies. The authors acknowledge the support to the research from: company Autodesk for WAAM 3D printing of the steel sheet; SoE Workshop technicians for coupon preparation; WMG (at Warwick University) for using their laboratory equipment for tensile testing and for XCT imagining. For the XCT scanning and imagine procesing we gratefully acknowledge funding from the Strategic Equipment - High Speed XCT EPSRC grant (EP/S010076/1).

The authors also express their appreciation to Mr Paul Hadlum (Test Engineer, WMG) for his support with coupon instrumentation, test data acquisition and for operating the Instron testing machines.

References

[1] M Sakin, YC Kiroglu, 3D printing of buildings: construction of the sustainable houses of the future by BIM, Energy Procedia 134 (2017) 702–711.
[2] T Duda, LV Raghavan, 3D metal printing technology, IFAC-PapersOnLine 2016 (49) (2016) 103–110, https://doi.org/10.1016/j.ifacol.2016.11.111.
[3] Bhavar V., Kattire P., Patil V., Khot S., Gujar K., Singh R, A review on powder bed fusion technology of metal additive manufacturing, In: 4th International conference and exhibition on Additive Manufacturing Technologies-AM-2014 (pp. 1-2).
[4] DD Camacho, P Clayton, P O'brien, R Ferron, M Juenger, S Salamone, C Seepersad, Applications of Additive Manufacturing in the Construction Industry – A Prospective Review. ISARC 34 (2017), https://doi.org/10.1016/j.ifacol.2016.11.111.
[5] B Berman, 3D printing: the new industrial revolution, Bus. Horiz. 55 (2012) 155–162, https://doi.org/10.1016/j.bushor.2011.11.003.
[6] P Wu, J Wang, X Wang, A critical review of the use of 3D printing in the construction industry, Autom. Constr. 68 (2016) 21–31, https://doi.org/10.1016/j.autcon.2016.04.005.
[7] N Mrazović, M Baumers, R Hague, M Fischer, Guiding building professionals in selecting additive manufacturing technologies to produce building components, Mate. Today Commun. 15 (2018) 199–202, https://doi.org/10.1016/j.mtcomm.2018.02.012.
[8] Skanska claims first with 3D printed cladding, Construction Manager, https://www.constructionmanagermagazine.com/news/skanska-claims-industry-first-3d-printed-cladding/, 2013 (accessed 1 April 2020).
[9] C Buchanan, V-P Matilainen, A Salminen, L Gardner, Structural performance of additive manufactured metallic material and cross-sections, J. Constr. Steel Res. 136 (2017) 35–48, https://doi.org/10.1016/j.jcsr.2017.05.002.
[10] M Ashraf, I Gibson, M Rashed G, Challenges and prospects of 3d printing in structural engineering, 13th International Conference on Steel, Space and Composite Structures (Perth, WA), Engineers Australia, 2018.
[11] S Galjaard, S Hofman, N Perry, S Ren, Optimizing structural building elements in metal by using additive manufacturing In: Proceedings of IASS Annual Symposia, International Association for Shell and Spatial Structures (IASS) 2 (2015) 1–12.
[12] L Wang, W Du, P He, M Yang, Topology Optimization and 3D Printing of Three-Branch Joints in Treelike Structures, J. Struct. Eng. 14604019167 (2020). https://orcid.org/0000-0002-3659-2613.
[13] AG Izard, RF Alfonso, G Mcknight, L Valdevit, Optimal design of a cellular material encompassing negative stiffness elements for unique combinations of stiffness and elastic hysteresis, Mater. Des. 135 (2017) 37–50, https://doi.org/10.1016/j.matdes.2017.09.001.
[14] Yalcinkaya G, World's first 3D-printed steel bridge unveiled at Dutch Design Week. https://www.dezeen.com/2018/10/22/worlds-first-3d-printed-steel-bridge-completed-mx3d-technology/?li_source=LI&li_medium=bottom_block_1, 2018(accessed 1 March 2020).
[15] Autodesk Introduces Mobile Additive Manufacturing Toolbox To 3D Print On Location. https://3dprint.com/231758/autodesk-introduce-mobile-am-toolbox/, 2018 (accessed 3 June 2020).
[16] DD Camacho, P Clayton, WJ O'Brien, C Seepersad, M Juenger, R Ferron, S Salamone, Applications of additive manufacturing in the construction industry–A forward-looking review, Autom. Constr. 89 (2018) 110–119, https://doi.org/10.1016/j.autcon.2017.12.031.
[17] BS EN 1993-1-1:2005+A1:2014. Design of steel structures, part 1-1 General rules and rules for buildings. 2005, British Standard Institute: London.
[18] JJ Lewandowski, M Seifi, Metal additive manufacturing: a review of mechanical properties, Annu. Rev. Mater. Res. 46 (2016) 151–186, https://doi.org/10.1146/annurev-matsci-070115-032024.
[19] Keating S, Beyond 3D Printing: The New Dimensions of Additive Fabrication. Designing for Emerging Technologies: UX for Genomics, Robotics, and the Internet of Things (2014) 379-405, O'Reilly Media. http://hdl.handle.net/1721.1/95739.
[20] C Gosselin, R Duballet, P Roux, N Gaudillière, J Dirrenberger, P Morel, Large-scale 3D printing of ultra-high performance concrete–a new processing route for architects and builders, Mater. Des. 100 (2016) 102–109, https://doi.org/10.1016/j.matdes.2016.03.097.
[21] M Zenou, L Grainger, Additive manufacturing of metallic materials, in: Additive Manufacturing, Butterworth-Heinemann, 2018, pp. 53–103.
[22] SW Williams, F Martina, AC Addison, J Ding, G Pardal, P Colegrove, Wire+ arc additive manufacturing, Mater. Sci. Technol. 32 (2016) 641–647, https://doi.org/10.1179/1743284715Y.0000000073.
[23] NR Baddoo, Castings in construction, Steel Construction Institute, 1996.
[24] BS EN 10002-1:2001. Tensile testing of metallic materials. Method of test at ambient temperature. British Standard Institute: London.

[25] A Lopez, R Bacelar, I Pires, TG Santos, JP Sousa, L Quintino, Non-destructive testing application of radiography and ultrasound for wire and arc additive manufacturing, Addit. Manuf. 21 (2018) 298–306, https://doi.org/10.1016/j.addma.2018.03.020.
[26] A Thompson, I Maskery, RK Leach, X-ray computed tomography for additive manufacturing: a review, Meas. Sci. Technol. 27 (2016) 072001.
[27] N Kourra, JM Warnett, A Attridge, G Dibling, J Mcloughlin, S Muirhead-Allwood, R King, M Williams, Computed tomography metrological examination of additive manufactured acetabular hip prosthesis cups, Addit. Manuf. 22 (2018) 146–152. https://doi.org/10.1016/j.addma.2018.04.033.
[28] I. McEwen, D.E. Cooper, J.M. Warnett, N. Kourra, M.A. Williams, G.J. Gibbons, Design & manufacture of a high-performance bicycle crank by additive manufacturing, Appl. Sci. 8 (8) (2018) 1360, https://doi.org/10.3390/app8081360.
[29] Weast RC, Density of Water(g/mL) vs. Temperature (oC). 1972 http://jupiter.plymouth.edu/~jsduncan/courses/2012_Spring/Techniques/Exams/DensityOfWater-vs-Temp.pdf. (accessed 15 April 2020).
[30] AB Spierings, M Schneider, R Eggenberger, Comparison of density measurement techniques for additive manufactured metallic parts, Rapid Prototyp. J. 17 (2011) 380–386, https://doi.org/10.1108/13552541111156504.
[31] BS EN 10025-1:2004. Hot-rolled products of structural steels- Part1: General technical delivery conditions. British Standard Institute: London.
[32] NA to BS EN 1993-1-1:2005:2008 UK National Annex to Eurocode 3: Design of steel structures. General rules and rules for buildings (+A1:2014), British Standard Institute: London.
[33] BS EN1990:2002+A1:2005. Eurocode 0 – Basis of Structural Design. British Standards Institute; London.
[34] D Roylance, Stress-Strain Curves, Massachusetts Institute of Technology study, Cambridge, 2001.
[35] M Eudier, The mechanical properties of sintered low-alloy steels, Powder Metall. 5 (1962) 278–290, https://doi.org/10.1179/pom.1962.5.9.005.
[36] RA Hardin, C Beckermann, Effect of porosity on the stiffness of cast steel, Metall. Mater. Trans. A 38 (2007) 2992–3006, https://doi.org/10.1007/s11661-007-9390-4.
[37] RA Hardin, C Beckermann, Effect of porosity on deformation, damage, and fracture of cast steel, Metall. Mater Trans. A 44 (2013) 5316–5332, https://doi.org/10.1007/s11661-013-1669-z.